

Near-Equilibrium Propagation training in nonlinear wave systems

Karol Sajnok^{1,*} and Michał Matuszewski^{1,2,†}

¹Center for Theoretical Physics, Polish Academy of Sciences, Aleja Lotników 32/46, 02-668 Warsaw, Poland

²Institute of Physics, Polish Academy of Sciences, Aleja Lotników 32/46, 02-668 Warsaw, Poland

(Dated: October 21, 2025)

Backpropagation learning algorithm, the workhorse of modern artificial intelligence, is notoriously difficult to implement in physical neural networks. Equilibrium Propagation (EP) is an alternative with comparable efficiency and strong potential for *in-situ* training. We extend EP learning to both discrete and continuous complex-valued wave systems. In contrast to previous EP implementations, our scheme is valid in the weakly dissipative regime, and readily applicable to a wide range of physical settings, even without well defined nodes, where trainable inter-node connections can be replaced by trainable local potential. We test the method in driven-dissipative exciton-polariton condensates governed by generalized Gross-Pitaevskii dynamics. Numerical studies on standard benchmarks, including a simple logical task and handwritten-digit recognition, demonstrate stable convergence, establishing a practical route to in-situ learning in physical systems in which system control is restricted to local parameters.

Neuromorphic learning performed directly in physical substrates promises orders-of-magnitude gains in throughput and energy efficiency by letting dynamics, rather than digital emulation, handle training and inference [1–6]. Optical and solid-state platforms—from photonic interferometers and memristive crossbars to spintronic oscillators, superconducting circuits, and Ising machines—offer reconfigurable couplings with fast, low-noise readout. Yet, end-to-end *in situ* training remains challenging because conventional backpropagation assumes an explicit computational graph and faithful adjoint—assumptions fragile in analog hardware with hidden couplings, latency, and dissipation [1, 7]. Driven-dissipative wave systems, such as photonic neural networks, are particularly attractive, combining extremely high throughput, scalability, and efficiency [5–9]. While *in silico* training yields good results for small systems, accumulated errors and model-experiment gaps in large setups demand efficient *in situ* algorithms. Recent breakthroughs include adjoint propagation, feedback alignment, physics-aware training, and forward-forward variants [10–15]. Still, complex-valued fields in nonlinear systems intertwine amplitude, phase, gain, loss, and spatiotemporal coupling, making it difficult to match digital backpropagation accuracy.

Equilibrium Propagation (EP) is an energy-based, biologically plausible algorithm offering a two-phase scheme for local gradient estimation via contrasts between free and nudged steady states [16]. In supervised learning, explicit backpropagation is replaced by steady-state contrasts: the system first relaxes under input drive, then under gentle nudging dependent on output error, with their difference defining parameter updates through a local rule. EP was shown equivalent to recurrent backpropagation [17, 18] and achieves state-of-the-art accuracy on large-scale digital tasks [18, 19]. It has been extended to deep convolutional, spiking, and oscillator networks [19–24], quantum systems [25–27], Lagrangian trajectory-based learning [28, 29], and agnostic learning in black-box physical systems [30]. Notably, EP was experimentally demonstrated in an Ising network on the D-Wave quantum circuit [31].

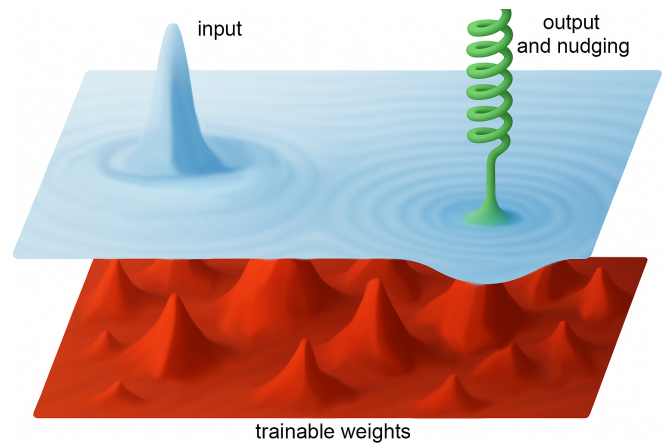


Figure 1: Scheme of NEP implementation in a continuous wave system (light blue) with input drive, output and nudging force (green spring) and trainable potential parameters (red).

Here, we introduce Near-Equilibrium Propagation (NEP), a generalization of EP to driven-dissipative complex-wave systems. A schematic illustration is shown in Fig. 1, indicating trainable potential parameters, input drive, output readout, and nudging in the output region. Our approach extends previous results in several ways: (i) operates in the near-equilibrium regime of weak pumping and dissipation; (ii) is applicable to oscillatory and wave systems, extending beyond conventional EP based on energy relaxation; (iii) can train *local parameters* instead of inter-node weights, thus covering a broader class of physical systems; and (iv) accommodates both discrete and continuous complex-valued fields. Some of these aspects were partially explored before. Generalization of EP to real-valued vector-field dynamics without a well-defined energy function was considered in [32]. Training oscillatory systems with EP was studied in [22–24], but those models assumed energy-gradient descent rather than Hamiltonian dynamics, yielding relaxation instead of oscillatory behavior. EP in complex networks was introduced in [19] for holomorphic functionals, which do not correspond to physi-

cal real-valued quantities like energy or Hamiltonian. In [33], the analogy between continuous wave systems and neural networks was recognized, but no method for in-situ training was provided, relying instead on backpropagation in a discretized digital model.

To test our theory, we numerically model NEP learning in exciton-polariton condensates, a unique platform combining light and matter [34–36]. Realizations of polariton neural networks include reservoir computing, binarized, and spiking networks [37–44]. Recent studies show that exciton-polaritons can achieve high energy efficiency in machine-learning inference [6, 45]. We demonstrate numerically stable NEP training on tasks such as logical XOR in one-dimensional lattices and MNIST digit classification in two-dimensional systems. We first derive NEP for general wavefunction dynamics and establish local update rules from free-nudged contrasts near equilibrium. Next, we model a feasible polariton implementation using the driven-dissipative Gross-Pitaevskii equation (GPE), describing pumping geometry, output-region nudging, and measurable observables. Finally, we show convergence and accuracy in numerical simulations and discuss experimental prospects and limitations.

Near-Equilibrium Propagation in complex-valued systems. We define the NEP learning protocol for driven-dissipative systems. An oscillatory or wave system is described by a time-dependent complex field $\psi(\vec{r}, t)$ defined over a spatial domain $\vec{r} \in \mathcal{M}$, which may be continuous or discrete depending on the physical realization.

Training proceeds via a two-step procedure for each input sample $\mathbf{X} = (x_1, x_2, \dots)$. In the first, free-evolution phase, the system follows

$$\partial_t \psi(\vec{r}, t) = \kappa_\psi(\psi(\vec{r}, t), \theta, \mathbf{X}), \quad (1)$$

where $\theta = (\theta_1, \theta_2, \dots)$ is the vector of trainable parameters, such as local potentials, inter-node couplings, or input weights. Unlike in conventional EP, Eq. (1) need not derive from a variational principle with an energy functional. We assume that after sufficiently long evolution, the system reaches an oscillating steady state $\psi(\vec{r}, t) = \Psi_0(\vec{r}) e^{i\omega t}$, where ω denotes frequency, implying $\kappa_0(\Psi_0(\vec{r}), \theta, \mathbf{X}) := \kappa_\psi e^{-i\omega t} = i\omega \Psi_0(\vec{r})$. We assume ω is locked to a resonant drive, $\omega = \omega_D = \text{const}$, independent of θ and \mathbf{X} . Moving to the rotating frame $\Psi(\vec{r}, t) = \psi(\vec{r}, t) e^{-i\omega_D t}$ gives

$$\partial_t \Psi(\vec{r}, t) = \kappa(\Psi(\vec{r}, t), \theta, \mathbf{X}) \stackrel{\text{s.s.}}{=} 0, \quad (2)$$

with $\kappa = \kappa_0(\Psi, \theta, \mathbf{X}) - i\omega_D \Psi$, where the last equality in (2) is fulfilled in the steady state $\Psi(\vec{r}, t) = \Psi_0(\vec{r})$.

In the second, nudged phase, the system is perturbed with respect to the target. The goal is to tune θ to minimize the cost function $C(\Psi_0)$, quantifying output-target discrepancy. To achieve this, we add a driving term proportional to the cost gradient

$$\partial_t \Psi = \kappa - i\beta \frac{\partial C(\Psi_0, \bar{\Psi}_0)}{\partial \bar{\Psi}_0} =: \kappa^\beta, \quad (3)$$

where β is a small real parameter and $\frac{\partial C}{\partial \bar{\Psi}}$ is a Wirtinger derivative. The perturbation includes an imaginary factor, and derivatives are taken with respect to the conjugate variable. This yields a simple in-situ gradient-descent rule. We assume the system relaxes to a new, nudged steady state satisfying $\kappa^\beta(\Psi, \theta, \mathbf{X}, \beta) \stackrel{\text{s.s.}}{=} 0$.

For complex-field systems, the output can depend on both amplitude and phase; here, we focus on amplitude. For instance, the mean-squared error (MSE) cost in the continuous case is

$$C_{\text{MSE}}(\Psi_0, \bar{\Psi}_0) = \frac{1}{2} \int_{\mathcal{Y}} (|\Psi_Y|^2 - |\Psi_0(\vec{r})|^2)^2 d\vec{r}, \quad (4)$$

where \mathcal{Y} is the output region. This choice leads, via Eq. (3), to the evolution equation

$$\kappa_{\text{MSE}}^\beta = \kappa + i\beta \Theta_{\mathcal{Y}} (|\Psi_Y|^2 - |\Psi_0|^2) \Psi_0, \quad (5)$$

with Heaviside step function $\Theta_{\mathcal{Y}}(\vec{r}) = 1$ for $\vec{r} \in \mathcal{Y}$ and 0 otherwise. Another example is the categorical cross-entropy (CCE) cost, useful for multi-class tasks, given in the discrete case by

$$C_{\text{CCE}}(\Psi_0, \bar{\Psi}_0) = - \sum_i |\Psi_Y(\vec{r}_i)|^2 \ln \sigma(|\Psi_0(\vec{r}_i)|^2), \quad (6)$$

where $\sigma(|\Psi(\vec{r}_i)|^2) = \frac{\exp(|\Psi(\vec{r}_i)|^2)}{\sum_j \exp(|\Psi(\vec{r}_j)|^2)}$ is the softmax function, and the sum runs over all output nodes $\vec{r}_i \in \mathcal{Y}$ corresponding to output classes. The nudged evolution then becomes

$$\kappa_{\text{CCE}}^\beta = \kappa + i\beta \sum_i (|\Psi_Y(\vec{r}_i)|^2 - \sigma(|\Psi_0(\vec{r}_i)|^2)) \Psi_0(\vec{r}_i). \quad (7)$$

Thus, the nudged perturbation depends on the chosen cost function and is confined to \mathcal{Y} .

Parameter updates θ can be applied per sample, batch, or epoch. They minimize the cost along the steepest gradient

$$\Delta \theta \propto - \left. \frac{\partial C}{\partial \theta} \right|_{\beta=0} = i \left\langle \frac{\partial \bar{\Psi}}{\partial \beta}, \frac{\partial \bar{\kappa}}{\partial \theta} \right\rangle - i \left\langle \frac{\partial \Psi}{\partial \beta}, \frac{\partial \kappa}{\partial \theta} \right\rangle, \quad (8)$$

where $\langle f, g \rangle$ is the inner product, $\langle f, g \rangle := \int_{\mathcal{M}} d\vec{r} \bar{f}(\vec{r}) g(\vec{r})$ in the continuous case, and $\langle f, g \rangle := \sum_{i \in \mathcal{M}} \bar{f}(\vec{r}_i) g(\vec{r}_i)$ in the discrete one. The derivation for both cases is given in Appendix A. This rule generalizes [32] and holds for any complex wave equation, provided derivatives of $\kappa(\Psi, \bar{\Psi}, \theta, \mathbf{X})$ satisfy near-equilibrium conditions

$$\frac{\partial \kappa(\vec{r})}{\partial \bar{\Psi}(\vec{s})} = \frac{\partial \kappa(\vec{s})}{\partial \bar{\Psi}(\vec{r})}, \quad \frac{\partial \kappa(\vec{r})}{\partial \Psi(\vec{s})} \approx - \frac{\partial \bar{\kappa}(\vec{s})}{\partial \bar{\Psi}(\vec{r})}. \quad (9)$$

Here, *equilibrium* is understood more broadly than in previous EP works [16, 22, 23], referring to a stationary fixed point of Eq. (2). When a Hamiltonian functional $H(\Psi, \bar{\Psi})$ exists such that $\kappa \approx i\{\Psi, H\} = i \frac{\partial H}{\partial \bar{\Psi}}$ with $\{\cdot\}$ as the Poisson bracket,

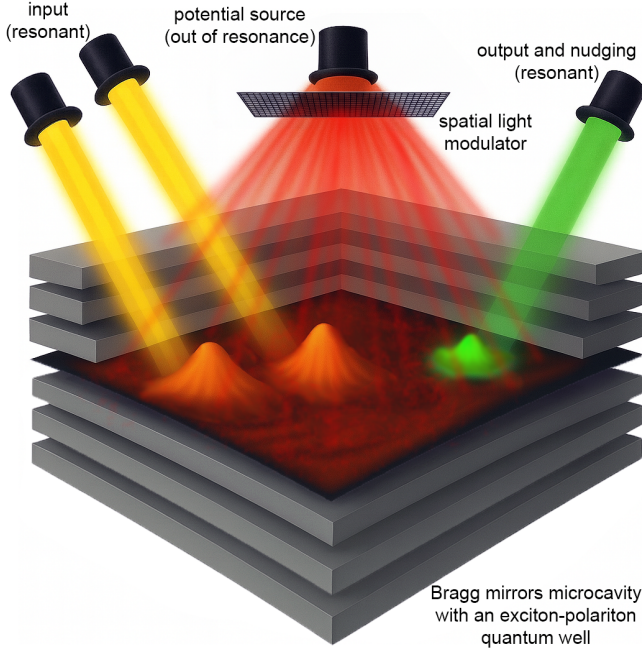


Figure 2: Example of a polaritonic system with two inputs and one output. Two localized laser beams (yellow) encode the inputs. A spatially modulated trainable potential (red) is applied via a spatial light modulator. The selected area (green) marks the output region where optical nudging and readout occur. Input and output beams share the same frequency ω_D .

Eq. (9) is naturally satisfied. As shown below, even when not exactly fulfilled, training can still converge successfully.

During inference, nudging β is switched off, and outputs are read directly from the steady-state amplitudes Ψ_Y in the output region, with the system driven by input X as in the free phase.

Implementation in exciton-polariton systems. Exciton-polariton systems are ideal for optical neural networks owing to their strong nonlinearity, ultrafast dynamics, and high energy efficiency [6, 38, 39, 45]. The NEP setup, shown in Fig. 2, consists of a cavity sample hosting polaritons, resonant laser beams for input pumping and output nudging, and a non-resonant laser forming the potential. Trainable parameters include both software input weights and the physical potential landscape controlled by a spatial light modulator.

For illustration, we adapt the general NEP framework to driven-dissipative polaritons described by a generalized continuous GPE with dissipation γ , complex potential $V(\vec{r})$, resonant pumping $P(\vec{r})$, and nonlinear function $f(\Psi)$ —either density response $f_d(\Psi) = g_d|\Psi|^2$ or saturation response $f_s(\Psi) = \frac{g_s}{1+|\Psi|^2}$. In the rotating frame, the polariton wavefunction $\Psi(\vec{r}, t)$ evolves as

$$\partial_t \Psi \equiv \kappa = -\frac{i}{\hbar} \left(-\frac{\hbar^2}{2m} \nabla^2 + V + f(\Psi) - i\gamma \right) \Psi + P, \quad (10)$$

where $P(\vec{r}) = \sum_k w_k X_k G(\vec{r} - \vec{r}_k)$, with complex input weights w_k for inputs X_k and normalized Gaussian envelopes $G(\vec{r} - \vec{r}_k) = \exp\left[-\frac{|\vec{r} - \vec{r}_k|^2}{2W^2}\right]$ of width W centered at \vec{r}_k . The complex potential $V(\vec{r})$ and pumping weights w_k constitute the trainable parameters θ . Although the terms P , γ , and $\text{Im} V$ break Hamiltonian dynamics, we show below that NEP remains accurate when γ and $\text{Im} V$ are small compared to the other terms (the near-equilibrium regime). The Laplacian term, being parity-symmetric, satisfies both conditions in Eqs. (9).

In the nudged evolution phase, the perturbation is introduced in the output region \mathcal{Y} , as defined in Eq. (4), depending on the chosen cost function. Experimentally, this corresponds to applying a resonant top-hat pump in \mathcal{Y} with amplitude proportional to the error and a $\frac{\pi}{2}$ phase shift relative to input pumps. The steady state $\Psi_0(\vec{r})$ satisfies $\kappa^\beta(\Psi^\beta, V, w, P, \beta) = 0$.

To determine update rules for the two training parameters—the potential $V(\vec{r})$ and pumping weights $w(\vec{r}_k)$ —we employ the NEP rule Eq. (8). Using the derivative of κ with respect to the real potential $V(\vec{r})$ gives

$$\Delta V(\vec{r}) \propto -\frac{\partial C}{\partial V(\vec{r})} = -\frac{1}{\hbar} \frac{\partial |\Psi_0(\vec{r})|^2}{\partial \beta}. \quad (11)$$

Analogously, for the real pump weights,

$$\Delta w_k \propto -\frac{\partial C}{\partial w_k} = -2 \int d\vec{r} X_k G(\vec{r} - \vec{r}_k) \text{Im} \frac{\partial \Psi_0(\vec{r})}{\partial \beta}. \quad (12)$$

Thus, updates for both the potential and pump weights depend on local steady-state fields $\Psi_0(\vec{r}, \beta)$ obtained in the free and driven phases. The parameter β controls the nudging strength and must be small enough for accurate derivative estimation at $\beta = 0$, yet large enough to induce a measurable change in the wavefunction.

Numerical results. In simulations, we use a discretized version of the GPE and implement the two-phase NEP algorithm on a finite spatial grid. In dimensionless units, the discretized GPE reads

$$\kappa_i = \frac{i}{2} (\Psi_{i+1} - 2\Psi_i + \Psi_{i-1}) - i(V_i + f(\Psi_i) - i\gamma)\Psi_i + P_i. \quad (13)$$

Dirichlet boundary conditions are imposed, realizable experimentally via a steep out-of-resonant potential wall, though the framework is independent of boundary choice. The evolution equation is integrated using a fourth-order Runge-Kutta (RK4) scheme.

As a proof of principle, we train a one-dimensional polariton network to implement the two-input XOR function. The simulation employs a 9-node grid, with two input nodes and one output node \mathcal{Y} . Figure 3 shows the system geometry and optimization results. Input samples X correspond to four binary combinations (00, 01, 10, 11) and are encoded as pump amplitudes $P_i = w_i (\delta_i^{11} X_1 + \delta_i^{12} X_2)$, where w_i are real input weights, and X_k ($k = 1, 2$) are the inputs located at sites

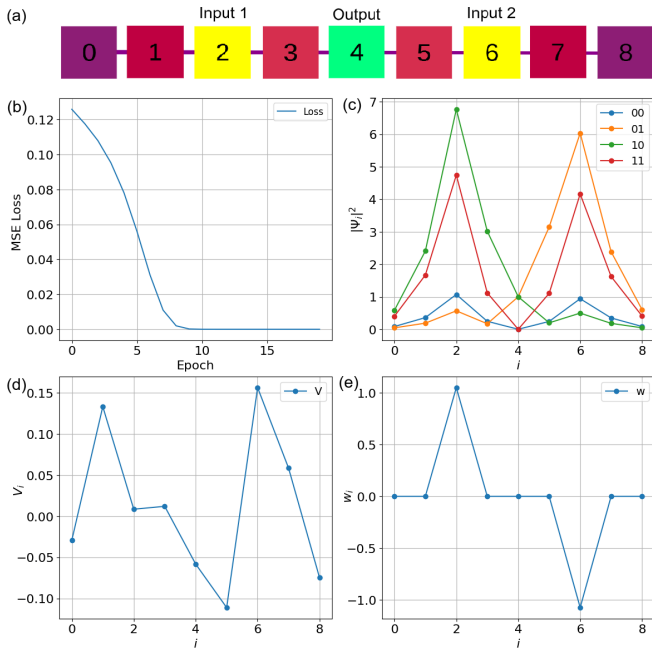


Figure 3: Training a 9-node 1D network for the 2-input XOR task. Inputs are applied symmetrically at sites 2 and 6, and the output is read at site 4 (a). Both potential V and pump weights w are trained. (b) Training loss; (c) steady-state field magnitudes $|\Psi_i|^2$ for each input; (e) trained potential V ; (d) pump weights w . Final outputs: $|\Psi_4|^2 = (0.00, 0.92, 1.06, 0.01)$ for inputs $(00, 01, 10, 11)$.

i_k . The target pattern Ψ_Y requires high amplitude ($|\Psi_Y|^2 = 1$) for $(01, 10)$ and low ($|\Psi_Y|^2 = 0$) otherwise. The cost function is the MSE between output intensity and target intensity for each input.

As shown in Fig. 3(b), convergence occurs after about 10 epochs with nudging parameter $\beta = 0.01$. Both potential V and pump weights w are trained following Eqs. (11)–(12), using learning rates $\text{lr}_V = \text{lr}_w = 0.1$. The GPE parameters are $g = 0.1$, $\gamma = 0.1$, and nonlinear saturation response $f_s(\Psi_i) = \frac{g_s}{1 + |\Psi_i|^2}$. Other panels of Fig. 3 show steady-state amplitudes, potential, and input weights in the trained system. Appendix B demonstrates that optimization remains effective regardless of input/output node positions and can rely on training both V_i and w_i , or only V_i with fixed w_i . The method is robust to random potential perturbations—e.g., structural inhomogeneities in experimental samples—verified by training with fixed small random fluctuations, which did not affect convergence.

To demonstrate the capability of the NEP algorithm to train multi-class classification tasks, we trained a 2D discrete polariton network to classify a five-digit subset of the MNIST handwritten digits dataset (1000 samples per digit), see Fig. 4. The simulation is performed on a 5×25 grid, where the input region \mathcal{X} corresponds to the entire network area, with each 3×3 cell receiving a copy of the same input. Input patterns are generated by resizing and normalizing MNIST images, fol-

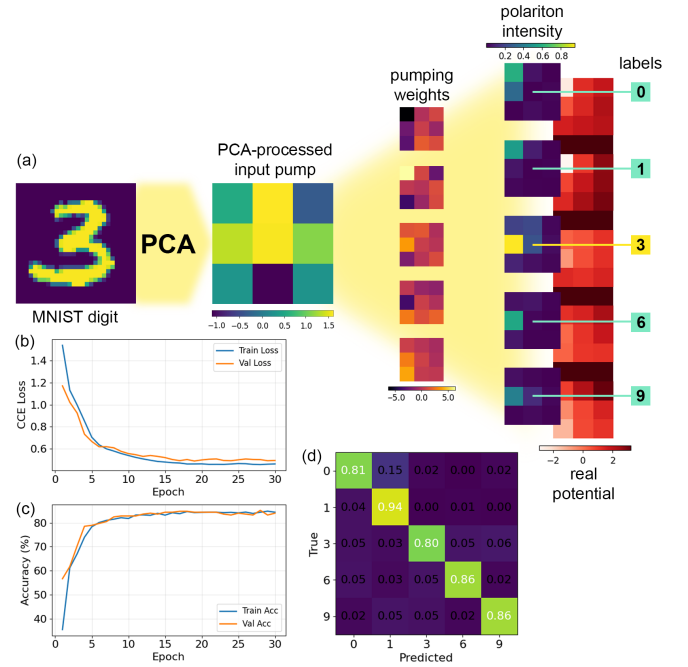


Figure 4: Training a 3×15 2D network to classify a subset of MNIST digits. Each of the five 3×3 cells receives a PCA-processed input image. The output region \mathcal{Y} contains five central nodes corresponding to digits 0, 1, 3, 6, 9. Panel (a): data flow including PCA transformation, replication, and optical injection. Cells are separated by a blocking potential (red). (b, c): training and validation losses and accuracies; (d): confusion matrix with final accuracies on test set.

lowed by principal component analysis (PCA) [46] with 25 components to fit the 5×5 input area. The output region \mathcal{Y} consists of five central nodes, each representing one class. The output pattern Ψ_Y is one-hot encoded, with each output node (out of 5) required to have high intensity ($\sigma(|\Psi_Y|^2) = 1$) for correct digit and low intensity ($\sigma(|\Psi_Y|^2) = 0$) for all others, with the cost function given by Eq. (6). Convergence to a test accuracy of $\approx 85\%$ is achieved after about 20 training epochs with nudging parameter $\beta = 0.01$, learning rates $\text{lr}_V = \text{lr}_w = 0.1$, GPE parameters $g = 0.001$, $\gamma = 0.1$, and density-response nonlinearity $f_d(\Psi_i) = |\Psi_i|^2$. Previous studies reported that oscillatory networks with local connections perform poorly on MNIST [23]. We attribute the improved performance to nonequilibrium wave dynamics, which overcome the locality of node couplings.

We also trained the system to recognize all ten digits 0–9 using a similar architecture (10 cells of size 5×5 , 500 samples per digit), achieving a slightly lower test accuracy of $\approx 75\%$ (Appendix B). Training only the potential, without optimizing pumping weights, reduces performance but confirms that optimization can proceed via purely optical, not electronic, updates (Appendix B). A benchmark fully connected digital network with 25 PCA inputs, no hidden neurons, and 10 outputs trained by backpropagation achieves $\approx 88\%$ accuracy on full

MNIST. The discrepancy stems from the physical system's nearest-neighbor couplings via the Laplacian term, making propagation from PCA inputs distance-dependent. Varying the nonlinearity constant g shows optimal performance for moderate $g = 0.01$, corresponding to $\frac{g|\Psi|^2}{\gamma} \sim 1$, yielding the lowest final loss and highest test accuracy (Appendix B).

Experimental outlook and summary. The NEP protocol can be experimentally realized with current polariton systems. Numerical simulations for the 5-digit MNIST task (1000 samples per digit) converge after about 20 epochs for $\gamma = 0.1$, requiring two steady-state measurements per sample, each with ~ 5000 RK4 steps and $dt = 0.1$. In physical units, the full training procedure completes within $T_{\text{phys}} \sim 0.1$ ms to 10 ms for typical $\frac{1}{\gamma_{\text{phys}}} \sim 1$ ps to 100 ps [34, 47], nearly six orders of magnitude faster than GPU-based numerical integration (NVIDIA GeForce RTX 2080 Ti, 11 GB). Thus, NEP provides both conceptual and substantial practical advantages.

We have presented the NEP scheme, which transforms a nonlinear wave system into a machine-learning device trained via steady-state contrasts. Unlike previous approaches, our algorithm operates near equilibrium, trains local parameters instead of inter-node weights, and applies to both discrete and continuous systems. The protocol uses standard optical tools—spatial light modulators and camera-based readouts—is robust to moderate inhomogeneities, and naturally supports tiling into weakly coupled cells for large-scale tasks. Altogether, these features make NEP a realistic framework for laboratory implementation, enabling in-situ, ultrafast, energy-efficient training on polaritonic hardware within experimental reach.

Acknowledgments. We thank Andrzej Opala for useful discussions. The authors acknowledge support from the European Union EIC Pathfinder project ‘Neuromorphic Polariton Accelerator’ (PolArt, ID 101130304) from the National Science Center, Poland grant 2021/43/B/ST3/00752.

Data availability. The data that support the findings of this article are openly available [48].

Appendix A: Derivation of the Update Rule. Continuous variable case. We derive the update rule for a trainable parameter $\theta(\vec{r})$ in an arbitrary complex wave system. Using the chain rule for functional derivatives, the derivative of the cost function $C(\Psi, \bar{\Psi})$ with respect to $\theta(\vec{r})$ reads

$$\frac{\partial C}{\partial \theta(\vec{r})} = \int d\vec{s} \left(\frac{\partial C}{\partial \Psi(\vec{s})} \frac{\partial \Psi(\vec{s})}{\partial \theta(\vec{r})} + \frac{\partial C}{\partial \bar{\Psi}(\vec{s})} \frac{\partial \bar{\Psi}(\vec{s})}{\partial \theta(\vec{r})} \right), \quad (14)$$

where integration is over the spatial domain \mathcal{M} , and $\Psi = \Psi(\theta, \bar{\theta})$, $\bar{\Psi} = \bar{\Psi}(\theta, \bar{\theta})$ are steady-state fields depending implicitly on θ and $\bar{\theta}$.

From Eq. (3),

$$\frac{\partial C}{\partial \Psi} = -i \frac{\partial \bar{\kappa}^\beta}{\partial \beta}, \quad (15)$$

so Eq. (14) becomes

$$\frac{\partial C}{\partial \theta(\vec{r})} = -i \int d\vec{s} \left(\frac{\partial \bar{\kappa}^\beta}{\partial \beta} \frac{\partial \Psi(\vec{s})}{\partial \theta(\vec{r})} - \frac{\partial \kappa^\beta}{\partial \beta} \frac{\partial \bar{\Psi}(\vec{s})}{\partial \theta(\vec{r})} \right), \quad (16)$$

since $\frac{\partial C}{\partial \bar{\Psi}} = \frac{\partial C}{\partial \Psi}$ for real-valued C .

In the nudged steady state, $\kappa^\beta(\Psi^\beta, \bar{\Psi}^\beta, \theta, \bar{\theta}, \beta) = 0$, where Ψ^β and $\bar{\Psi}^\beta$ depend explicitly on $\theta, \bar{\theta}, \beta$. Treating these as independent variables and differentiating with respect to β yields

$$\frac{\partial \kappa^\beta(\vec{s})}{\partial \beta} = - \int d\vec{u} \left(\frac{\partial \kappa^\beta(\vec{s})}{\partial \Psi^\beta(\vec{u})} \frac{\partial \Psi^\beta(\vec{u})}{\partial \beta} + \frac{\partial \kappa^\beta(\vec{s})}{\partial \bar{\Psi}^\beta(\vec{u})} \frac{\partial \bar{\Psi}^\beta(\vec{u})}{\partial \beta} \right), \quad (17)$$

evaluated at $\beta = 0$.

Similarly, differentiating the stationary condition with respect to $\theta(\vec{r})$ gives

$$\frac{\partial \kappa^\beta(\vec{u})}{\partial \theta(\vec{r})} = - \int d\vec{s} \left(\frac{\partial \kappa^\beta(\vec{u})}{\partial \Psi^\beta(\vec{s})} \frac{\partial \Psi(\vec{s})}{\partial \theta(\vec{r})} + \frac{\partial \kappa^\beta(\vec{u})}{\partial \bar{\Psi}^\beta(\vec{s})} \frac{\partial \bar{\Psi}(\vec{s})}{\partial \theta(\vec{r})} \right), \quad (18)$$

also evaluated at $\beta = 0$. These relations describe how variations in β or θ propagate through steady-state fields via the system's linearized response near equilibrium.

Using Eq. (17), we expand Eq. (16), exchange integration order, and regroup terms by their β derivatives

$$\begin{aligned} \frac{\partial C}{\partial \theta(\vec{r})} = & i \int d\vec{u} \int d\vec{s} \\ & \left[\left(\frac{\partial \bar{\kappa}^\beta(\vec{s})}{\partial \bar{\Psi}^\beta(\vec{u})} \frac{\partial \Psi(\vec{s})}{\partial \theta(\vec{r})} - \frac{\partial \kappa^\beta(\vec{s})}{\partial \Psi^\beta(\vec{u})} \frac{\partial \bar{\Psi}(\vec{s})}{\partial \theta(\vec{r})} \right) \frac{\partial \Psi^\beta(\vec{u})}{\partial \beta} \right. \\ & \left. + \left(\frac{\partial \bar{\kappa}^\beta(\vec{s})}{\partial \bar{\Psi}^\beta(\vec{u})} \frac{\partial \Psi(\vec{s})}{\partial \theta(\vec{r})} - \frac{\partial \kappa^\beta(\vec{s})}{\partial \bar{\Psi}^\beta(\vec{u})} \frac{\partial \bar{\Psi}(\vec{s})}{\partial \theta(\vec{r})} \right) \frac{\partial \bar{\Psi}^\beta(\vec{u})}{\partial \beta} \right]. \end{aligned} \quad (19)$$

Assuming that derivatives of $\bar{\kappa}^\beta$ with respect to Ψ^β are invariant under spatial transposition and that the near-equilibrium conditions hold,

$$\frac{\partial \bar{\kappa}^\beta(\vec{s})}{\partial \Psi^\beta(\vec{u})} = \frac{\partial \bar{\kappa}^\beta(\vec{u})}{\partial \Psi^\beta(\vec{s})}, \quad \frac{\partial \kappa^\beta(\vec{s})}{\partial \Psi^\beta(\vec{u})} \approx - \frac{\partial \bar{\kappa}^\beta(\vec{u})}{\partial \bar{\Psi}^\beta(\vec{s})}, \quad (20)$$

comparison of Eqs. (18) and (19) gives

$$\frac{\partial C}{\partial \theta(\vec{r})} \approx -i \int d\vec{u} \left(\frac{\partial \bar{\kappa}^\beta(\vec{u})}{\partial \theta(\vec{r})} \frac{\partial \Psi(\vec{u})}{\partial \beta} - \frac{\partial \kappa^\beta(\vec{u})}{\partial \theta(\vec{r})} \frac{\partial \bar{\Psi}(\vec{u})}{\partial \beta} \right), \quad (21)$$

evaluated at $\beta = 0$.

Gross-Pitaevskii Equation. Returning to the polariton GPE, we now write the update rule explicitly. Condition (20) holds when the imaginary part of the potential $V(\vec{r})$ and the dissipation parameter γ are negligible (near-equilibrium regime),

since the Liouvillian is spatially symmetric and the diagonal Jacobians are

$$\frac{\partial \kappa^\beta(\vec{u})}{\partial \Psi(\vec{s})} = \left(\frac{i\hbar}{2m} \nabla^2 - i\frac{V}{\hbar} - i\frac{2g}{\hbar} |\Psi(\vec{u})|^2 - \frac{\gamma}{\hbar} \right) \delta(\vec{s} - \vec{u}), \quad (22)$$

$$\frac{\partial \bar{\kappa}^\beta(\vec{u})}{\partial \bar{\Psi}(\vec{s})} = - \left(\frac{i\hbar}{2m} \nabla^2 - i\frac{\bar{V}}{\hbar} - i\frac{2g}{\hbar} |\Psi(\vec{u})|^2 + \frac{\gamma}{\hbar} \right) \delta(\vec{s} - \vec{u}), \quad (23)$$

where $\delta(\vec{s} - \vec{u})$ is the Dirac delta function. For an arbitrary nonlinearity $f(\Psi)$, condition (20) remains valid when

$$f(\Psi) + \Psi \frac{\partial f(\Psi)}{\partial \Psi} = \bar{f}(\Psi) + \bar{\Psi} \frac{\partial \bar{f}(\Psi)}{\partial \bar{\Psi}}. \quad (24)$$

Discrete variable case. In the discretized system, the derivation simplifies. Define the state vector $s = (\Psi_i, \bar{\Psi}_i)$ and evolution vector $K = (-i\kappa_i^\beta, i\bar{\kappa}_i^\beta)$. Using Eq. (15) and $K(s, \theta, \beta) \equiv 0$, we find

$$\Delta\theta_i \propto -\frac{\partial C}{\partial \theta_i} = -\frac{\partial C}{\partial s_j} \frac{\partial s_j}{\partial \theta_i} = \frac{\partial \bar{K}_j}{\partial \beta} \frac{\partial s_j}{\partial \theta_i} = -\frac{\partial \bar{K}_j}{\partial s_k} \frac{\partial s_k}{\partial \beta} \frac{\partial s_j}{\partial \theta_i}.$$

Under transposition invariance and the near-equilibrium condition, which now have the compact form

$$\frac{\partial \bar{K}_j}{\partial s_k} \approx \frac{\partial \bar{K}_k}{\partial s_j}, \quad (25)$$

and using again $K(s, \theta, \beta) \equiv 0$, we obtain

$$\begin{aligned} \Delta\theta_i &\propto -\frac{\partial \bar{K}_k}{\partial s_j} \frac{\partial s_k}{\partial \beta} \frac{\partial s_j}{\partial \theta_i} = \frac{\partial \bar{K}_k}{\partial \theta_i} \frac{\partial s_k}{\partial \beta} \\ &= i \frac{\partial \bar{\kappa}_k}{\partial \theta_i} \frac{\partial \Psi_k}{\partial \beta} - i \frac{\partial \kappa_k}{\partial \theta_i} \frac{\partial \bar{\Psi}_k}{\partial \beta}. \end{aligned} \quad (26)$$

Appendix B: Additional Simulation Results. XOR task. Figure 5(a)–(c) shows XOR training on the same 9-node architecture as in the main text, but with optimization limited to the potential V . Pump weights w are fixed near optimal ($w_2 = 1$, $w_6 = -0.75$), serving as static input encoding. Even under this restriction, the network minimizes loss and reproduces correct outputs, confirming that proper input encoding via w enables V -only training, though convergence saturates earlier and performance is less stable than with both V and w optimized.

Figure 5(d)–(f) presents a reduced 7-node network with asymmetric input placement (sites 1 and 3) and output at site 5, where both V and w are trained. Results show that spatial symmetry of inputs is unnecessary—the network still performs the XOR mapping under asymmetric geometry. This illustrates NEP’s robustness to architectural variation.

MNIST task. Figure 6 presents classification of the MNIST (10-digits) dataset using a 5×50 polariton grid with ten 5×5 input cells and ten output nodes. Training both V and w yields

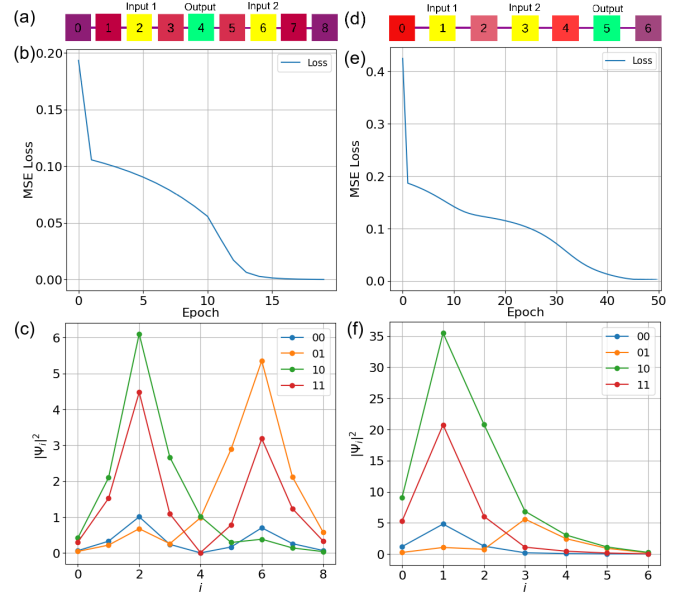


Figure 5: XOR task in (a) a 9-node 1D network with training restricted to V , fixed near-optimal pump weights w , and (d) a 7-node network with asymmetric input placement (sites 1, 3) and output at site 5. Top panels: training losses (b) for (a) and (e) for (d). Bottom: steady-state field magnitudes $|\Psi|^2$ for each input (c) and (f). (a)–(c) show that V -only training solves XOR for near-optimal fixed w ; (d)–(f) show successful training despite broken spatial symmetry.

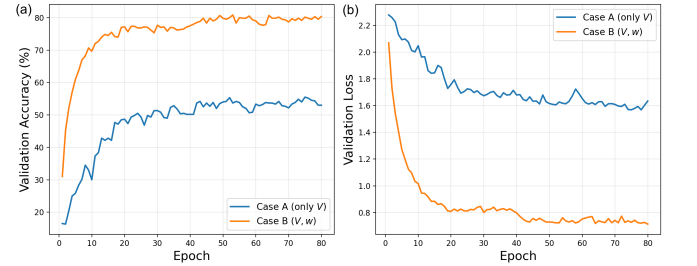


Figure 6: Impact of the choice of trainable parameters, V and w , on (a) validation accuracies and (b) CCE losses versus epochs during training of a 5×50 -node 2D network on MNIST (10-digits) using NEP for 50 epochs. Classification achieves $\sim 80\%$ accuracy when both V and w are trainable, and $\sim 53\%$ when w is fixed to unities.

$\approx 80\%$ test accuracy, confirming feasibility for 10-class problems. Training only V reaches $\approx 53\%$, still demonstrating purely optical optimization. Figure 7 shows the effect of nonlinearity g : moderate $g = 0.01$ ($\frac{g|\Psi|^2}{\gamma} \sim 1$) gives the best accuracy and stability, while larger g destabilizes learning, highlighting the need for careful nonlinearity tuning in quantum systems.

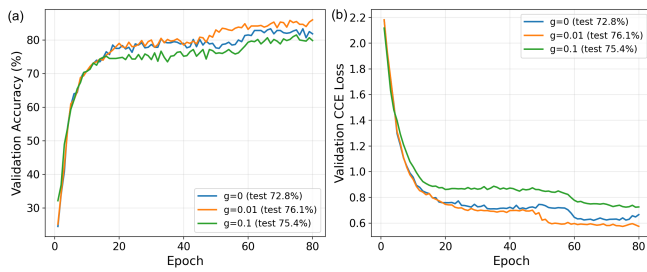


Figure 7: Effect of nonlinearity g on MNIST classification with a 5×50 polariton network. (a) Training accuracy; (b) training loss. Moderate $g = 0.01$ gives the most accurate learning, while larger g leads to poor convergence.

* ksajnok@cft.edu.pl

† mmatuszewski@cft.edu.pl

- [1] D. Marković, A. Mizrahi, D. Querlioz, and J. Grollier, *Nature Reviews Physics* **2**, 499 (2020).
- [2] V. K. Sangwan and M. C. Hersam, *Nature nanotechnology* **15**, 517 (2020).
- [3] J. Grollier, D. Querlioz, K. Y. Camsari, K. Everschor-Sitte, S. Fukami, and M. D. Stiles, *Nature Electronics* **3**, 360 (2020).
- [4] D. Kudithipudi, C. Schuman, C. M. Vineyard, T. Pandit, C. Merkel, R. Kubendran, J. B. Aimone, G. Orchard, C. Mayr, R. Benosman, *et al.*, *Nature* **637**, 801 (2025).
- [5] B. J. Shastri, A. N. Tait, T. Ferreira de Lima, W. H. Pernice, H. Bhaskaran, C. D. Wright, and P. R. Prucnal, *Nature Photonics* **15**, 102 (2021).
- [6] M. Matuszewski, A. Prystupiuik, and A. Opala, *Physical Review Applied* **21**, 014028 (2024).
- [7] A. Momeni, B. Rahmani, B. Scellier, L. G. Wright, P. L. McMahon, C. C. Wanjura, Y. Li, A. Skalli, N. G. Berloff, T. Onodera, *et al.*, *Nature* **645**, 53 (2025).
- [8] P. L. McMahon, *Nature Reviews Physics* **5**, 717 (2023).
- [9] G. Wetzstein, A. Ozcan, S. Gigan, S. Fan, D. Englund, M. Soljačić, C. Denz, D. A. Miller, and D. Psaltis, *Nature* **588**, 39 (2020).
- [10] T. W. Hughes, M. Minkov, Y. Shi, and S. Fan, *Optica* **5**, 864 (2018).
- [11] M. Nakajima, K. Inoue, K. Tanaka, Y. Kuniyoshi, T. Hashimoto, and K. Nakajima, *Nature communications* **13**, 7847 (2022).
- [12] L. G. Wright, T. Onodera, M. M. Stein, T. Wang, D. T. Schachter, Z. Hu, and P. L. McMahon, *Nature* **601**, 549 (2022).
- [13] I. Oguz, J. Ke, Q. Weng, F. Yang, M. Yildirim, N. U. Dinc, J.-L. Hsieh, C. Moser, and D. Psaltis, *Optics Letters* **48**, 5249 (2023).
- [14] S. Pai, Z. Sun, T. W. Hughes, T. Park, B. Bartlett, I. A. Williamson, M. Minkov, M. Milanizadeh, N. Abebe, F. Morichetti, *et al.*, *Science* **380**, 398 (2023).
- [15] A. Momeni, B. Rahmani, M. Malléjac, P. Del Hougne, and R. Fleury, *Science* **382**, 1297 (2023).
- [16] B. Scellier and Y. Bengio, *Frontiers in Computational Neuroscience* **11**, 24 (2017).
- [17] B. Scellier and Y. Bengio, *Neural Computation* **31**, 312 (2019).
- [18] M. Ernout, J. Grollier, D. Querlioz, Y. Bengio, and B. Scellier, in *Advances in Neural Information Processing Systems (NeurIPS)*, Vol. 32 (Curran Associates, Inc, 2019).
- [19] A. Laborieux, M. Ernout, B. Scellier, Y. Bengio, J. Grollier, and D. Querlioz, *Frontiers in neuroscience* **15**, 633674 (2021).
- [20] E. Martin, M. Ernout, J. Laydevant, S. Li, D. Querlioz, T. Petrisor, and J. Grollier, *Iscience* **24**(3), 102222 (2021).
- [21] L. S. Ricco, E. Imos, A. Opala, and H. Sigurðsson (2025), *Conference talk at OECS 19, Warsaw*.
- [22] T. Rageau and J. Grollier, *Neuromorphic Computing and Engineering* **5**, 034008 (2025).
- [23] Q. Wang, C. C. Wanjura, and F. Marquardt, *Neuromorphic Computing and Engineering* **4**, 034014 (2024).
- [24] G. Zoppo, F. Marrone, M. Bonnin, and F. Corinto, in *2022 IEEE International Symposium on Circuits and Systems (IS-CAS)* (2022) pp. 639–643.
- [25] B. Scellier, [arXiv:2406.00879](https://arxiv.org/abs/2406.00879) (2024).
- [26] S. Massar and B. M. Mognetti, *Quantum Studies: Mathematics and Foundations* **12**, 6 (2025).
- [27] C. C. Wanjura and F. Marquardt, *Nature Communications* **16**, 6595 (2025).
- [28] B. Scellier, [arXiv:2103.09985](https://arxiv.org/abs/2103.09985) (2021).
- [29] S. Massar, *Physical Review E* **112**, 035304 (2025).
- [30] B. Scellier, S. Mishra, Y. Bengio, and Y. Ollivier, [arXiv:2205.15021](https://arxiv.org/abs/2205.15021) (2022).
- [31] J. Laydevant, D. Marković, and J. Grollier, *Nature Communications* **15**, 3671 (2024).
- [32] B. Scellier, A. Goyal, J. Binas, T. Mesnard, and Y. Bengio, [arXiv:1808.04873](https://arxiv.org/abs/1808.04873) (2018).
- [33] T. W. Hughes, I. A. Williamson, M. Minkov, and S. Fan, *Science advances* **5**, eaay6946 (2019).
- [34] T. Byrnes, N. Y. Kim, and Y. Yamamoto, *Nature Physics* **10**, 803 (2014).
- [35] D. Sanvitto and S. Kéna-Cohen, *Nature materials* **15**, 1061 (2016).
- [36] M. D. Fraser, S. Höfling, and Y. Yamamoto, *Nature materials* **15**, 1049 (2016).
- [37] A. Opala, S. Ghosh, T. C. Liew, and M. Matuszewski, *Physical Review Applied* **11**, 064029 (2019).
- [38] D. Ballarini, A. Gianfrate, R. Panico, A. Opala, S. Ghosh, L. Dominici, V. Ardizzone, M. De Giorgi, G. Lerario, G. Gigli, *et al.*, *Nano Letters* **20**, 3506 (2020).
- [39] R. Mirek, A. Opala, M. Król, H. Suchomel, Ł. Kłopotowski, and *et al.*, *Nano Letters* **21**, 7214 (2021).
- [40] A. Kavokin, T. C. Liew, C. Schneider, P. G. Lagoudakis, S. Klemmt, and S. Hoefling, *Nature Reviews Physics* **4**, 435 (2022).
- [41] A. Opala and M. Matuszewski, *Optical Materials Express* **13**, 2674 (2023).
- [42] K. Tyszka, M. Furman, R. Mirek, M. Król, A. Opala, B. Serebyński, J. Szczytko, W. Pacuski, M. Matuszewski, and B. Piętka, *Laser & Photonics Reviews* **17**, 2370001 (2023).
- [43] A. Opala, R. Panico, V. Ardizzone, B. Piętka, J. Szczytko, D. Sanvitto, M. Matuszewski, and D. Ballarini, *Physical Review Applied* **18**, 024028 (2022).
- [44] A. Opala, K. Tyszka, M. Kędziora, M. Furman, A. Rahmani, S. Świerczewski, M. Ekielski, A. Szerling, M. Matuszewski, and B. Piętka, [arXiv:2412.10865](https://arxiv.org/abs/2412.10865) (2024).
- [45] M. Matuszewski, A. Opala, R. Mirek, M. Furman, M. Król, K. Tyszka, T. C. H. Liew, D. Ballarini, D. Sanvitto, J. Szczytko, and B. Piętka, *Physical Review Applied* **16**, 024045 (2021).
- [46] S. Wold, K. Esbensen, and P. Geladi, *Chemometrics and Intelligent Laboratory Systems* **2**, 37 (1987).
- [47] H. Deng, H. Haug, and Y. Yamamoto, *Reviews of Modern Physics* **82**, 1489 (2010).
- [48] K. Sajnok and M. Matuszewski, [10.5281/zenodo.1736940](https://zenodo.org/record/1736940) (2025).